Journal of *Marine Science and Engineering*

MDPI

Article

Experimental Investigation of the Platform and Tendon Dynamics of a 16 MW TLP Floating Wind Turbine

Qunyi Wang [1,2,3], Yingping Yu [4], Xu Han [1,2,3,*], Wendeng Yang [4], Chunzheng Li [2,5], Guangyuan Cheng [4], Linyang Cao [2,5] and Wei Shi [2,3,5,*]

1 Institute of Earthquake Engineering, Faculty of Infrastructure Engineering, Dalian University of Technology, Dalian 116024, China; qunyiwang@mail.dlut.edu.cn
2 State Key Laboratory of Coastal and Offshore Engineering, Dalian University of Technology, Dalian 116024, China; lichunzheng@mail.dlut.edu.cn (C.L.); caolinyang@mail.dlut.edu.cn (L.C.)
3 Key Laboratory of Integrated Development and Safety Assurance for Deep-Sea Energy and Resources, Ningbo Institute of Dalian University of Technology, Ningbo 315016, China
4 Beijing New Energy Branch, CNOOC (China) Limited, Beijing 102209, China; yuyp@cnooc.com.cn (Y.Y.); yangwd1@cnooc.com.cn (W.Y.); chenggy5@cnooc.com.cn (G.C.)
5 Deepwater Engineering Research Center, Offshore Renewable Energy Research Center, Dalian University of Technology, Dalian 116024, China
* Correspondence: xu.han@dlut.edu.cn (X.H.); weishi@dlut.edu.cn (W.S.)

Abstract

This study experimentally investigates the platform motions and tendon tensions of a 16 MW tension leg platform (TLP) floating wind turbine. A 1:85 hybrid model was tested under free-decay, regular-wave, irregular-wave, and combined wind–wave conditions. Under irregular waves, increasing the peak period enhanced the surge and heave dynamic responses but reduced the tension fluctuations of the selected tendons, whereas increasing the significant wave height enhanced both platform and tendon dynamic responses. Combined wind–wave loading introduced mean offsets in surge and pitch and altered the mean tension distribution among the selected tendons. The surge dynamic response remained close to the corresponding wave-only response, whereas the heave dynamic response showed a clear increase under combined wind–wave loading. The mean values of surge and pitch reached their largest measured values at the rated wind speed of 12 m/s, whereas the pitch and tendon dynamic responses became more pronounced at higher wind speeds. Frequency-domain analysis suggests possible coupling between the upwave tendon and platform pitch near the measured pitch natural frequency of approximately 0.249 Hz. Another possible coupling is indicated between the selected lateral tendons and the tower second mode within 2.1–2.2 Hz. The experimental results provide valuable insights into the platform and tendon dynamics of large-capacity TLP floating wind turbines and support their dynamic-response assessment under wave and combined wind–wave loading.

Keywords: floating offshore wind turbine; tension leg platform; hybrid model testing; tendon tension; dynamic response; frequency-domain analysis

Check for updates

Academic Editor: Eugen Rusu

Received: 16 September 2026
Revised: 27 October 2026
Accepted: 27 October 2026
Published: 31 October 2026

Copyright: © 2026 by the authors. Licensee MDPI, Basel, Switzerland. This article is an open access article distributed under the terms and conditions of the Creative Commons Attribution (CC BY) license.

1. Introduction

The development of offshore wind energy toward deeper waters has increased the demand for floating support structures [1]. The upscaling of wind turbine size requires careful assessment of the coupled dynamic response of floating wind turbines [2]. Among the available floating concepts, tension leg platforms (TLPs) use pretensioned tendons to provide station keeping and high vertical restoring stiffness [3,4]. This configuration

strongly constrains heave, roll, and pitch, whereas the platform remains relatively compliant in horizontal motion [3,5,6]. The dynamics of platform motions and tendon tensions should therefore be thoroughly evaluated, especially with the influences of the wind turbine and its load [7].

Wave-basin model tests provide experimental data for characterizing the responses of floating wind turbines and validating numerical models [8–11]. Such experiments enable simultaneous measurements of platform motions and mooring-system responses under controlled environmental conditions [10,11]. Previous experimental studies have included free-decay, regular-wave, and irregular-wave tests [5,6,9–11]. More recent studies have extended model testing by incorporating hybrid aerodynamic loading for a 10 MW turbine model [12] and real-time turbine control for a 15 MW turbine model [13].

Experimental studies have characterized platform motions and tendon tensions of TLP floating wind turbines under wave and combined environmental conditions [5,6,14,15]. Zhao et al. tested a multi-column WindStar TLP model in still water, white-noise waves, irregular waves, and combined wind–wave–current conditions [14]. Oguz et al. investigated TLPWIND through model tests and numerical comparisons, with aerodynamic thrust reproduced by a fan [5]. Murfet and Abdussamie reported response amplitude operators (RAOs) for platform motions and tendon tensions using a model with non-rotating blades [6]. An RAO is defined as the ratio of the response amplitude at the wave frequency to the incident-wave amplitude, with its units determined by the response quantity. Madsen et al. showed that turbine control affected surge response and tendon tensions in a scaled DTU 10 MW TLP [15]. Hmedi et al. used a software-in-the-loop method to reproduce rotor thrust and moments in 10 MW CENTEC-TLP model tests [16]. Other studies have addressed numerical model validation against experimental data [17,18] and high-frequency responses associated with second-order wave loading [19]. Ren et al. reported increased tensions in adjacent tendons after tendon failure, despite limited changes in platform motions under the tested conditions [20].

Physical model testing of floating wind turbines must account for the conflicting requirements of the hydrodynamic and aerodynamic scaling [21,22]. Wave-basin models generally follow Froude similarity, whereas reproducing rotor aerodynamics also requires consideration of Reynolds-number effects [22–24]. Froude and Reynolds similarity generally cannot be achieved simultaneously in geometrically scaled models using the same fluids as the prototype [22,24]. In hybrid wave-basin testing, aerodynamic loads are computed numerically based on turbine operating conditions and measured platform motions [23,25,26]. An actuation system then applies the scaled loads to the physical model [23,25,26]. Hybrid loading systems have been extended beyond rotor thrust to reproduce multiple aerodynamic load components [12,27,28]. Hybrid testing has also been reported for 15 MW turbine models [29]. Fu et al. [30] developed and evaluated a multi-degree-of-freedom loading device for real-time hybrid model testing of floating offshore wind turbines. The present paper focuses on the experimental investigations of the dynamics of this TLP and tendons under various environmental conditions.

Recent relevant studies have examined the responses in extreme and storm conditions [31,32], tendon inclination [33], and the design of a 22 MW system [34]. Other studies have investigated control effects [35] and responses under combined wind–wave–current loading [36]. These studies cover a range of TLP configurations and loading conditions and provide a useful basis for comparing platform motions and tendon tensions. A focused comparison within a single test campaign can clarify whether these responses exhibit similar sensitivities to wave period, significant wave height, and wind speed. Of particular interest is whether wind-induced changes in mean responses are accompanied by corresponding changes in response fluctuations. Higher-frequency TLP responses have

also been investigated under higher-order hydrodynamic loading and storm excitation, including responses associated with second-order sum-frequency wave loads [19,32,37,38]. The frequency-dependent relationships between tendon tensions and platform or tower responses also warrant examination across different tendon locations.

Accordingly, this study presents a series of 1:85-scale hybrid model tests of a 16 MW TLP floating wind turbine. Regular-wave tests compare the period dependence of response amplitude operators (RAOs) for platform motions and tendon tensions. Under wave-only conditions, irregular-wave tests assess the effects of peak period and significant wave height on response fluctuations. Combined wind–wave tests examine mean platform motions, the distribution of mean tendon tensions, and response fluctuations across the tested wind-speed range. Power spectral density analyses characterize the frequency content of the measured responses. Magnitude-squared coherence analyses examine the frequency-dependent associations of tendon tensions with platform motions and tower-top acceleration. These analyses focus on a representative combined wind–wave condition, with particular attention to differences among tendon locations. The resulting experimental findings provide a useful reference for future investigations of TLP dynamic responses under comparable loading conditions.

2. Experimental Methodology

2.1. Physical Model and Scaling

A 1:85-scale physical model of a 16 MW tension leg platform (TLP) floating wind turbine was used in the experiments. The prototype TLP configuration and principal dimensions were based on the design reported by Yang et al. [31]. The same physical model was used in the companion hybrid-testing study [39]. The model was designed according to Froude similarity with a geometric scale ratio of $\lambda = 85$ [21,39]. The principal prototype-to-model scaling relationships are listed in Table 1, and the principal properties at prototype and model scales are summarized in Table 2.

Table 1. Froude scaling relationships used in the model tests.

Quantity	Prototype/Model Scaling Ratio
Length	λ
Mass	λ^3
Time/period	$\lambda^{1/2}$
Frequency	$\lambda^{-1/2}$
Velocity	$\lambda^{1/2}$
Acceleration	1
Force	λ^3
Moment	λ^4

The corresponding principal properties at prototype and model scales are summarized in Table 2.

The model comprises the rotor–nacelle assembly, tower, multi-column TLP floater, and tendon system. The floater retains the triangular multi-column arrangement of the prototype. Nine vertical pretensioned tendons are arranged in three groups, with three tendons in each group, and are denoted T1–T9 throughout this paper. Figure 1 shows the assembled model and tendon arrangement.

Table 2. Principal properties of the 16 MW TLP at prototype and model scales.

Parameter	Prototype	Model
Water depth	134.25 m	1.58 m
Rotor–nacelle assembly (RNA) mass	764,000 kg	1.244 kg
Tower mass	1,399,000 kg	2.278 kg
Central-column diameter	16.154 m	0.190 m
Side-column diameter	15.687 m	0.185 m
Center distance between central and side columns	44.799 m	0.527 m
Number of tendons	9	9
Tendon length	110.250 m	1.297 m
Tendon axial stiffness	2.600×10^6 kN	4.234 kN

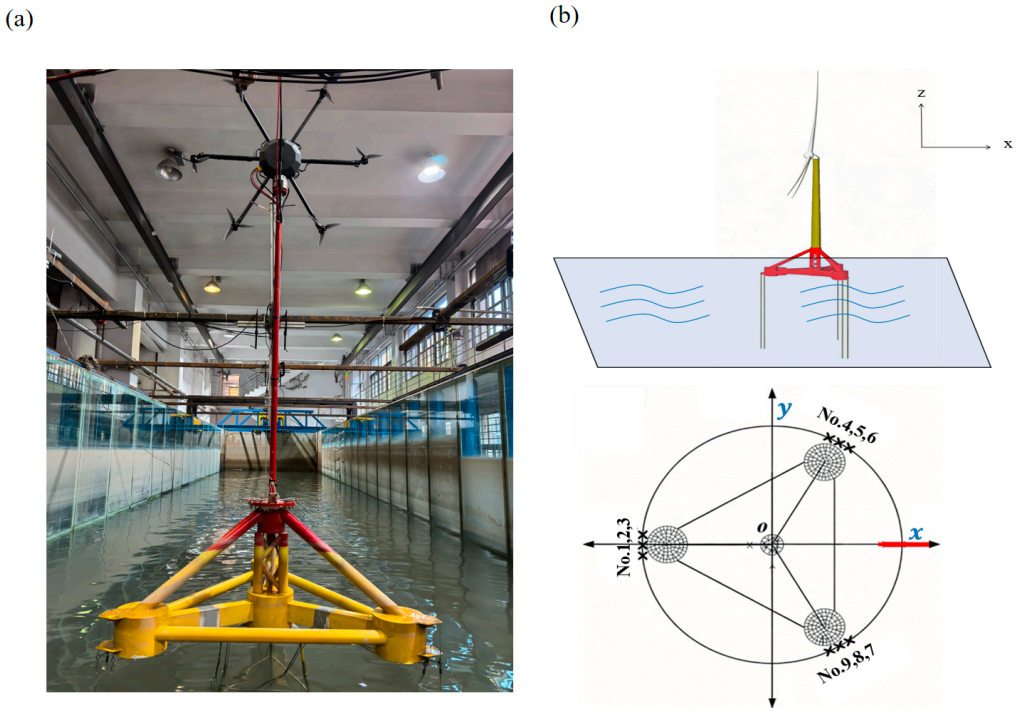


Figure 1. Physical model of the 16 MW TLP floating wind turbine: (**a**) overall view of the 1:85-scale model; (**b**) plan view showing the arrangement and numbering of the nine tendons and the global coordinate system.

2.2. Experimental Setup and Instrumentation

The experiments were conducted in the wave basin of the State Key Laboratory of Coastal and Offshore Engineering at Dalian University of Technology. The basin is 50 m long, 4 m wide, and 3 m deep, with a maximum operating water depth of 1.8 m. The test water depth in the basin was 1.58 m, corresponding to 134.25 m at prototype scale. Wind and wave directions were aligned in the combined tests.

Aerodynamic loading was reproduced using a six-rotor aerodynamic loading device mounted at the tower top. Target aerodynamic loads were calculated from prescribed turbine operating inputs and measured six-degree-of-freedom platform motions. The target load set comprised F_x, M_x, M_y, and M_z, which were reproduced by the loading device. A separate six-component force sensor was installed between the six-rotor aerodynamic loading device and the tower to measure the forces and moments transmitted to the tower,

including F_x, F_y, F_z, M_x, M_y, and M_z. The F_x, M_x, M_y, and M_z were compared with their corresponding target values to assess the agreement between the applied and target aerodynamic loads. The aerodynamic-load calculation and the implementation and validation of the hybrid loading system are described in detail in the companion study [39].

Under two representative combined wind–wave conditions, the Q–Q coefficients of determination between the measured and target aerodynamic loads ranged from 0.988 to 0.996 for thrust and from 0.927 to 0.979 for aerodynamic moments, while the PSD-weighted magnitude-squared coherence values ranged from 0.904 to 0.990. The system operated at 50 Hz using one-step-ahead prediction and asynchronous command release to reduce execution-related delays. The measured command-release latency was below 1 ms, although this value does not represent the total closed-loop delay.

The available validation results showed good agreement in the dominant loading characteristics, but the residual phase lag and its individual influence on the measured responses were not independently quantified.

At the system-response level, the reported statistical errors between the experimental and OpenFAST results for surge, heave, pitch, and the upwind-center tendon tension did not exceed 9.6% under the two validation conditions. These results support the reliability of the principal coupled responses within the validated conditions.

Platform motions, tendon tensions, wave elevation, aerodynamic loads, and tower-top x-acceleration were measured during the tests. Tendon load cells were installed at the platform fairleads to measure the tensions in T1–T9. Wave gauges were arranged along the wave-propagation direction, as shown in Figure 2a, and an accelerometer was mounted at the tower top to measure the x-direction acceleration. The corresponding instrumentation and measured channels are summarized in Table 3. Further information on the measurement accuracies of the optical motion-capture system and tendon load cells, as well as the calibration of the six-component force sensor, is provided in the companion study.

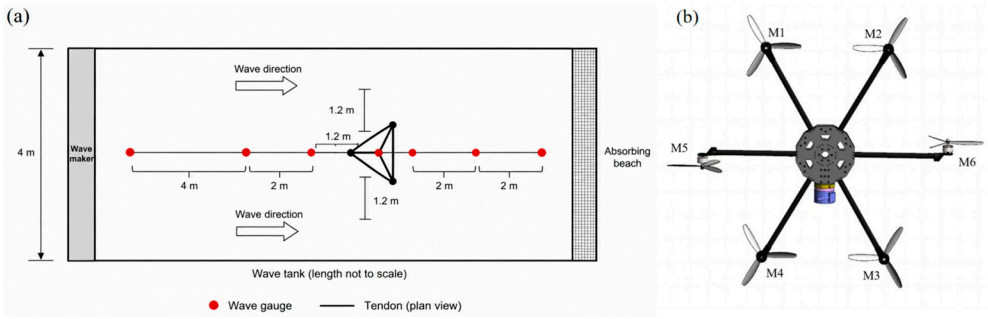


Figure 2. Experimental setup: (**a**) wave-basin arrangement and TLP model location; (**b**) six-rotor aerodynamic loading device.

Table 3. Measured quantities and instrumentation.

Measured Quantity	Instrumentation	Measured Channels/Locations
Platform motion	NDI optical motion-capture system	Surge, sway, heave, roll, pitch, yaw
Tendon tension	Load cells	T1–T9
Wave elevation	Wave gauges	Free-surface elevation
Aerodynamic loads	Six-component force sensor	*Fx*,*Fy*,*Fz*,*Mx*,*My*,*Mz*
Structural acceleration	Accelerometers	Tower top

The positive x-direction was defined along the wind and wave propagation direction, and the positive z-direction was defined vertically upward. Positive surge and F_x share the same direction, and the sign convention for M_y is consistent with that for pitch. Tendon tension is reported as positive throughout the paper. All measurement systems were synchronized based on absolute timestamps.

2.3. Test Program and Environmental Conditions

The test program comprised free-decay, regular-wave, irregular-wave, and combined wind–wave tests. Environmental parameters and response quantities are reported at prototype scale according to the Froude scaling relationships in Table 1. Free-decay tests were conducted in still water for all six rigid-body degrees of freedom to determine the natural periods presented in Section 3.1.

The regular-wave tests were conducted without aerodynamic loading. Wave heights of 4 and 5 m were selected to compare the responses at two excitation levels, while wave periods of 8–15 s were used to systematically examine the period dependence of the platform-motion and tendon-tension RAOs. The selection also considered the 1:85 scale ratio and the wave-generation capabilities of the basin to ensure reliable wave generation at model scale. The test conditions are summarized in Table 4.

Table 4. Regular-wave test conditions at prototype scale.

Wave Height, H (m)	Wave Period, T (s)
4	8, 9, 10, 11, 12, 13, 14, 15
5	8, 9, 10, 11, 12, 13, 14, 15

Irregular waves were generated using a JONSWAP spectrum [40]. Two test series were conducted by varying one wave parameter at a time. The first varied T_p at fixed $H_s = 5$ m, and the second varied H_s at fixed $T_p = 10$ s. An additional wave-only condition at $H_s = 6$ m and $T_p = 12$ s was included as the corresponding wave-only reference for the representative combined wind–wave condition. The irregular-wave conditions are listed in Table 5.

Table 5. Irregular-wave test conditions at prototype scale.

Purpose	H_s (m)	T_p (s)
Peak-period variation	5	10, 12, 14, 16
Significant-wave-height variation	4, 5, 6	10
Reference wave-only condition	6	12

The combined wind–wave tests comprised three series with one environmental parameter varied at a time. Peak period was varied at fixed $U = 12$ m/s and $H_s = 5$ m, whereas significant wave height was varied at fixed $U = 12$ m/s and $T_p = 10$ s. Wind speed was varied at fixed $H_s = 5$ m and $T_p = 12$ s. The rated wind speed was 12 m/s. The representative combined wind–wave condition used for the frequency-domain analyses was $U = 12$ m/s, $H_s = 6$ m, and $T_p = 12$ s. The combined test conditions are summarized in Table 6.

Regular and irregular waves were calibrated from wave-gauge measurements before the corresponding response tests. All forced-response analyses were performed over the prototype-scale interval of 500–3000 s after excluding the initial transient period.

Table 6. Combined wind–wave test conditions at prototype scale.

Purpose	Wind Speed, U (m/s)	H_s (m)	T_p (s)
Peak-period variation	12	5	10, 12, 14, 16
Significant-wave-height variation	12	4, 5, 6	10
Wind-speed variation	8, 12, 15, 18, 21	5	12
Representative combined condition	12	6	12

Each test condition was repeated three times. For repeated irregular-wave tests, the same prescribed JONSWAP wave realization was used with an identical random seed. A representative valid record was selected for the reported response analyses rather than averaging the repeated time series.

For the irregular-wave and combined wind–wave tests, platform-motion standard deviations (STDs) were calculated after zero-phase filtering with a fourth-order Butterworth low-pass filter at 1.0 Hz (prototype scale), whereas tendon-tension STDs were calculated from the unfiltered records. The low-pass filtering was intended to mitigate potential high-frequency measurement noise and experimental disturbances in the platform-motion signals. The regular-wave response amplitude operators (RAOs) and power spectral densities (PSDs) were calculated from unfiltered signals.

The repeatability of the irregular-wave tests was assessed for the six distinct conditions in the two parameter-variation series using the coefficient of variation (CV) of the response STDs obtained from three repeated tests. The CVs ranged from 0.06% to 3.01% across surge, heave, pitch, and the selected tendon tensions (T2, T5, and T6). A comparison of filtered and unfiltered platform-motion records for these conditions showed that filtering reduced the surge and heave STDs by less than 0.12% and the pitch STDs by 3.14–4.87%.

3. Results and Discussion

3.1. Free-Decay Tests

Free-decay tests were conducted in still water to determine the natural periods of the assembled 16 MW TLP model. Table 7 summarizes the measured periods at prototype scale. The same dataset was used for the experimental–numerical assessment reported in the companion study [39].

Table 7. Measured natural periods from the free-decay tests.

Degree of Freedom	Natural Period (s)
Surge	32.37
Sway	33.07
Heave	1.97
Roll	4.08
Pitch	4.01
Yaw	19.34

The natural periods in Table 7 reflect the different restoring characteristics of the TLP. Horizontal translations are relatively compliant, whereas tendon restraint results in much shorter natural periods in heave, roll, and pitch. The measured surge, heave, and pitch natural periods also provide reference frequencies for interpreting the regular-wave and frequency-domain responses discussed below.

3.2. Regular-Wave Tests

Regular-wave tests were used to characterize the dependence of platform-motion and tendon-tension RAOs on wave period. Response amplitudes at the wave frequency $f = 1/T$ were extracted from the raw records using harmonic least-squares fitting. Platform-motion RAOs were calculated as the response amplitude at the wave frequency divided by the measured incident-wave amplitude [9]. The surge and heave RAOs are dimensionless, whereas the pitch RAO is expressed in deg/m.

Figure 3 shows the platform-motion RAOs for wave heights of 4 and 5 m. The surge RAO increases monotonically from approximately 0.25–0.28 at $T = 8$ s to 1.21 at $T = 15$ s. The heave RAO varies non-monotonically between approximately 0.008 and 0.011. The pitch RAO ranges from approximately 0.037 to 0.055 deg/m, with no monotonic dependence on wave period. For each motion component, the RAOs at the two wave heights remain close over the tested period range.

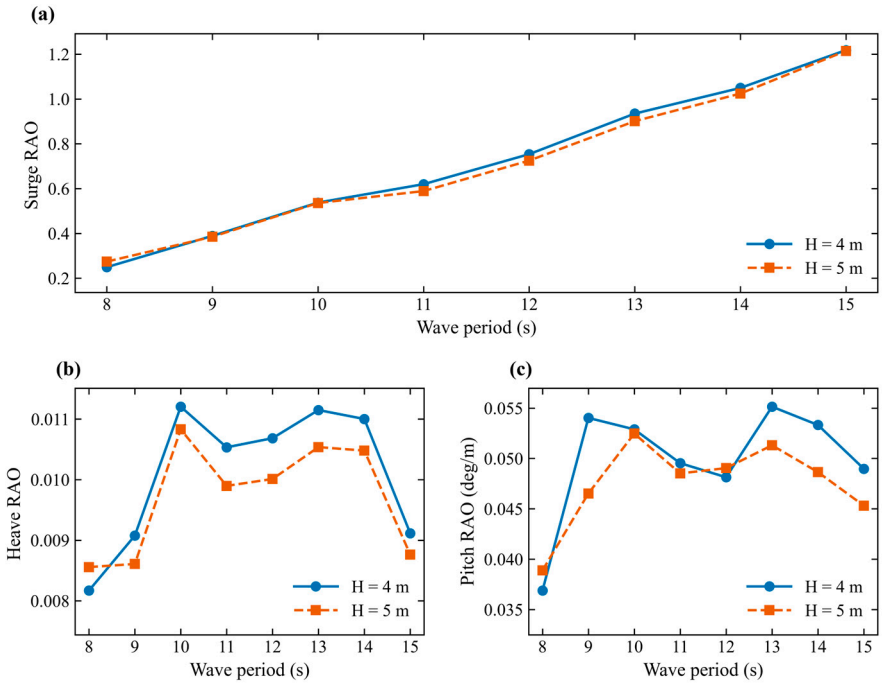


Figure 3. Platform-motion RAOs under regular waves at $H = 4$ and 5 m: (**a**) surge; (**b**) heave; (**c**) pitch.

Tendon-tension RAOs were calculated by dividing the tension amplitude at the wave frequency, ΔT_a, by the measured incident-wave amplitude, a, giving units of MN/m [6,9]. T2 and T1 are the central and adjacent tendons of the upwave group, respectively. T5 and T6 are the central and adjacent tendons of the lateral group. Figure 4 shows that all four tendon RAOs increase to maxima at periods of approximately 9–10 s and then decrease. The maximum values range from approximately 0.55 to 0.70 MN/m, with T1 and T5 exhibiting larger maxima than T2 and T6. The RAOs at the two wave heights remain generally close.

The different trends in Figures 3 and 4 indicate distinct period-dependent characteristics of the surge and tendon-tension RAOs over the tested range. Numerical investigations of tendon inclination also show that mooring geometry affects both platform motions and tension fluctuations [33]. Murfet and Abdussamie [6] reported similar period-dependent trends in surge and tendon RAOs, whereas the present surge and tendon-tension RAOs reach their maxima at different wave periods. This comparison suggests that the relative trends of platform-motion and tendon-tension RAOs can depend on the TLP configuration and loading conditions.

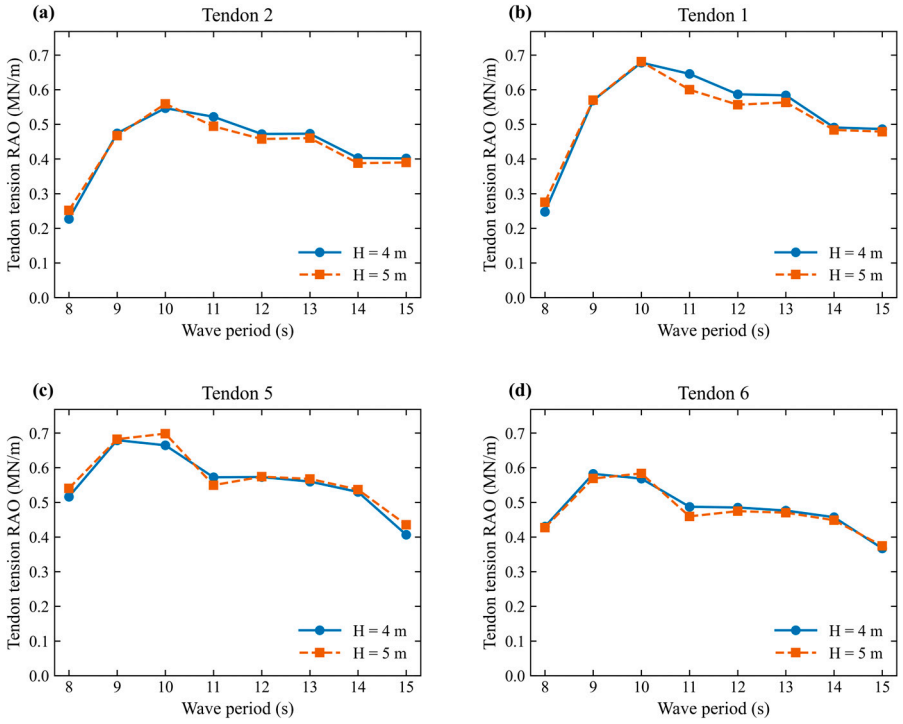


Figure 4. Tendon-tension RAOs under regular waves at H = 4 and 5 m: (**a**) T2; (**b**) T1; (**c**) T5; (**d**) T6.

3.3. Irregular-Wave Tests

Irregular-wave tests were used to characterize the effects of peak period and significant wave height on response fluctuations. The tendon-tension STDs were expressed as percentages of the corresponding measured static pretensions, T_0 [15]. Results are presented for T2 in the upwave group and T5 and T6 in the lateral group.

Figure 5 shows the response STDs at H_s = 5 m. As T_p increases from 10 to 16 s, the surge STD increases from approximately 0.73 to 1.66 m. The heave STD also increases from approximately 0.011 to 0.019 m. The pitch STD remains within approximately 0.061–0.064 deg, with no monotonic trend. In contrast, the normalized tendon-tension STDs decrease from approximately 7.8–10.0% to 6.8–8.2%. T5 has the largest normalized tension STD among the three tendons throughout the tested period range.

Figure 6 shows increasing platform-motion and tendon-tension STDs with increasing H_s at T_p = 10 s. As H_s increases from 4 to 6 m, the surge STD rises from approximately 0.62 to 0.87 m. The heave and pitch STDs increase from approximately 0.010 to 0.014 m and from 0.050 to 0.071 deg, respectively. The normalized tendon-tension STDs increase from approximately 6.2–7.9% to 9.4–11.8%.

The contrasting trends in Figures 5 and 6 can be related to changes in the dominant wave-excitation period and the frequency dependence of the responses. At fixed significant wave height, increasing the peak period shifts the dominant wave excitation toward longer periods. Within the overlapping period range, this shift is consistent with increasing surge RAOs and decreasing tendon RAOs in Figures 3 and 4. At fixed peak period, increasing significant wave height increases the wave-energy level without shifting the spectral peak. These observations provide a qualitative link between the regular- and irregular-wave results. They do not establish that first-order wave-frequency response accounts for the full variance.

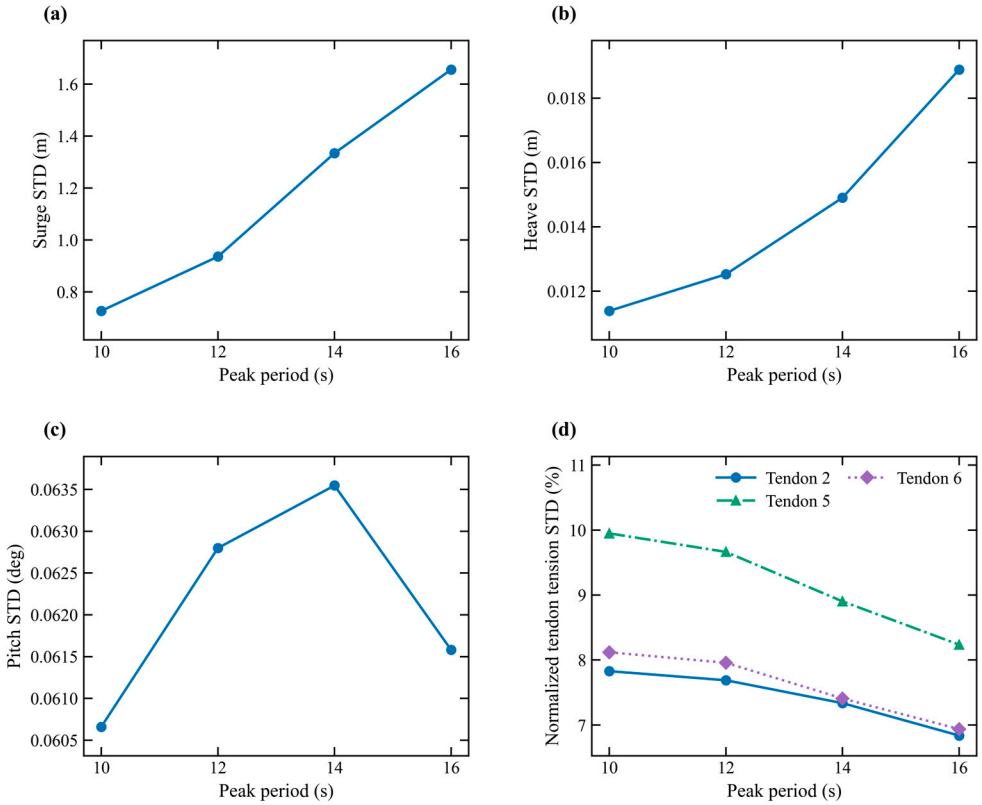


Figure 5. Standard deviations under irregular waves at $H_s = 5$ m: (**a**) surge; (**b**) heave; (**c**) pitch; (**d**) normalized tendon tension.

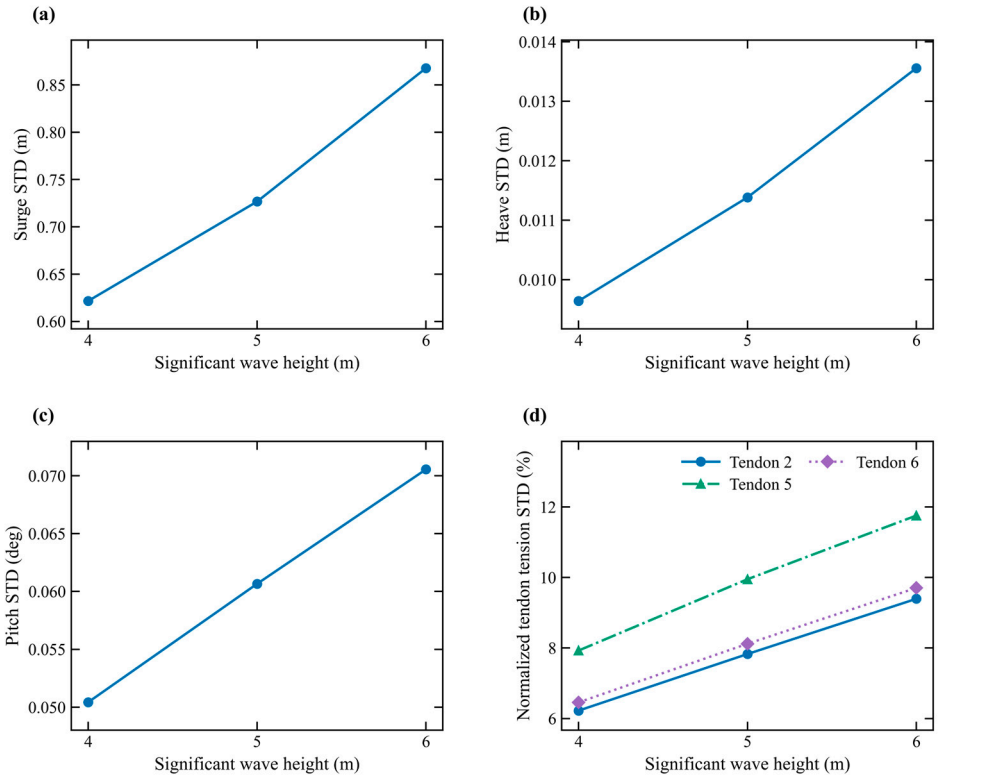


Figure 6. Standard deviations under irregular waves at $T_p = 10$ s: (**a**) surge; (**b**) heave; (**c**) pitch; (**d**) normalized tendon tension.

3.4. Combined Wind–Wave Tests

Figure 7 compares the responses under wave-only and combined wind–wave conditions at $U = 12$ m/s. Across both the peak-period and significant-wave-height series, the mean values of surge under combined loading remain approximately 2.74–2.90 m, whereas the corresponding values under wave-only loading remain approximately 0.03–0.07 m. For each motion component, the STD ratio is defined as the STD under combined wind–wave loading divided by that under the corresponding wave-only condition. The STD ratio for surge remains approximately 0.90–1.06. The STD ratios for heave and pitch range from approximately 1.49 to 2.22 and from 1.13 to 1.29, respectively. Thus, combined wind–wave loading produces a pronounced increase in the mean value of surge, whereas the STD of surge changes only slightly, and the STDs of heave and pitch increase relative to the corresponding wave-only conditions.

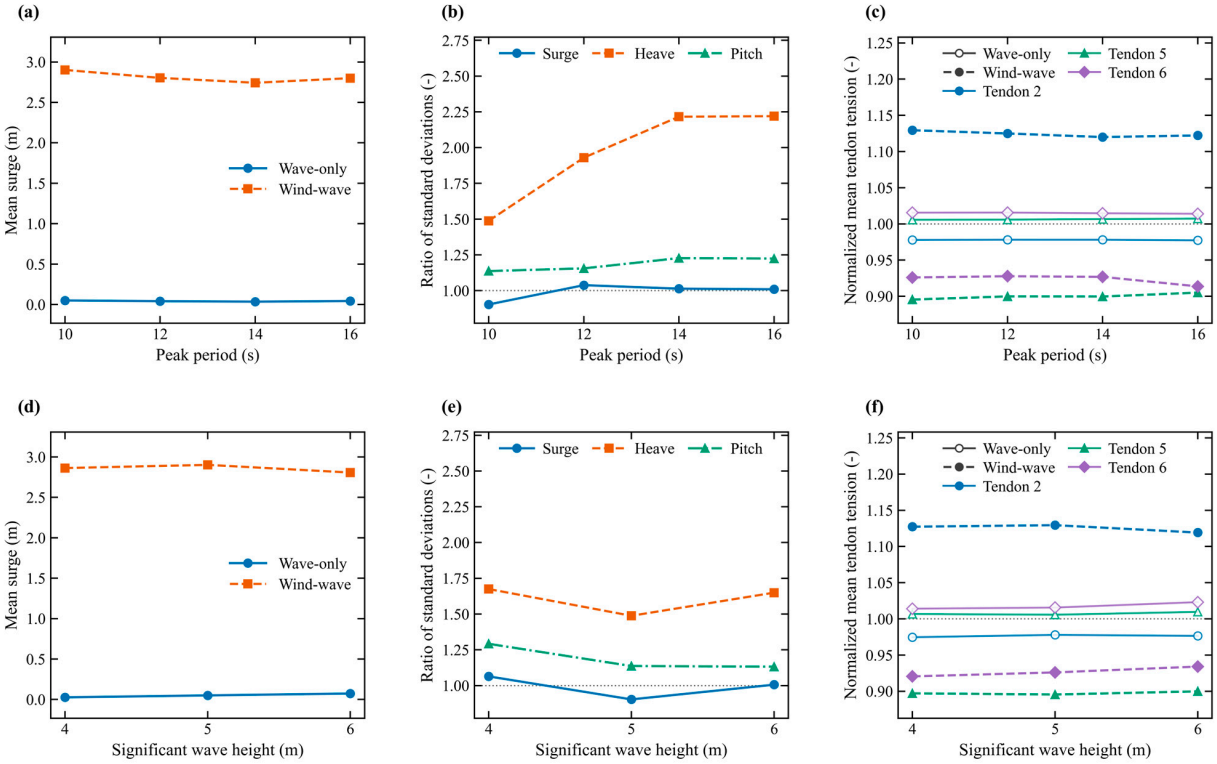


Figure 7. Wave-only and combined wind–wave responses at $U = 12$ m/s: (**a**) mean value of surge, (**b**) STD ratios of platform motions, and (**c**) normalized mean values of tendon tension for the T_p series at $H_s = 5$ m; (**d**) mean value of surge, (**e**) STD ratios of platform motions, and (**f**) normalized mean values of tendon tension for the H_s series at $T_p = 10$ s.

The mean value of tendon tension is normalized by the measured static pretension, T_0 as T/T_0 [5]. Under combined loading, the normalized values for T2 remain above unity, whereas those for T5 and T6 remain below unity. The corresponding normalized values under wave-only conditions remain close to unity. These results indicate that the mean value of tendon tension in T2 is higher than its static pretension, whereas the corresponding mean values in T5 and T6 are lower than their static pretensions.

The differences in the mean values of tendon tension in Figure 7 are consistent with a change in the equilibrium loading of the tendon system under combined wind–wave loading. Changes in platform position and attitude can modify the equilibrium tension distribution of the tendon system. Oguz et al. [5] similarly reported that platform trim had a pronounced influence on the mean values of the front and rear tendon tensions in TLPWIND, whereas the side tendon tensions were less affected by platform drift. These

differences among T2, T5, and T6 indicate a change in the equilibrium tendon-tension distribution under combined loading.

Figure 8 shows the variations in platform and tendon responses with wind speed at $H_s = 5$ m and $T_p = 12$ s. The wave-only condition at $H_s = 5$ m and $T_p = 12$ s is used as the reference for all STD ratios of platform motions. The mean value of surge increases from approximately 2.19 m at $U = 8$ m/s to 2.80 m at the rated wind speed of 12 m/s. The mean value of pitch follows the same trend. It increases from approximately 0.171 deg at $U = 8$ m/s to 0.205 deg at $U = 12$ m/s and then decreases to 0.128 deg at $U = 21$ m/s. Similarly reported non-monotonic trends in the mean values of surge and pitch for TLPWIND, with maxima occurring near the rated wind speed [5].

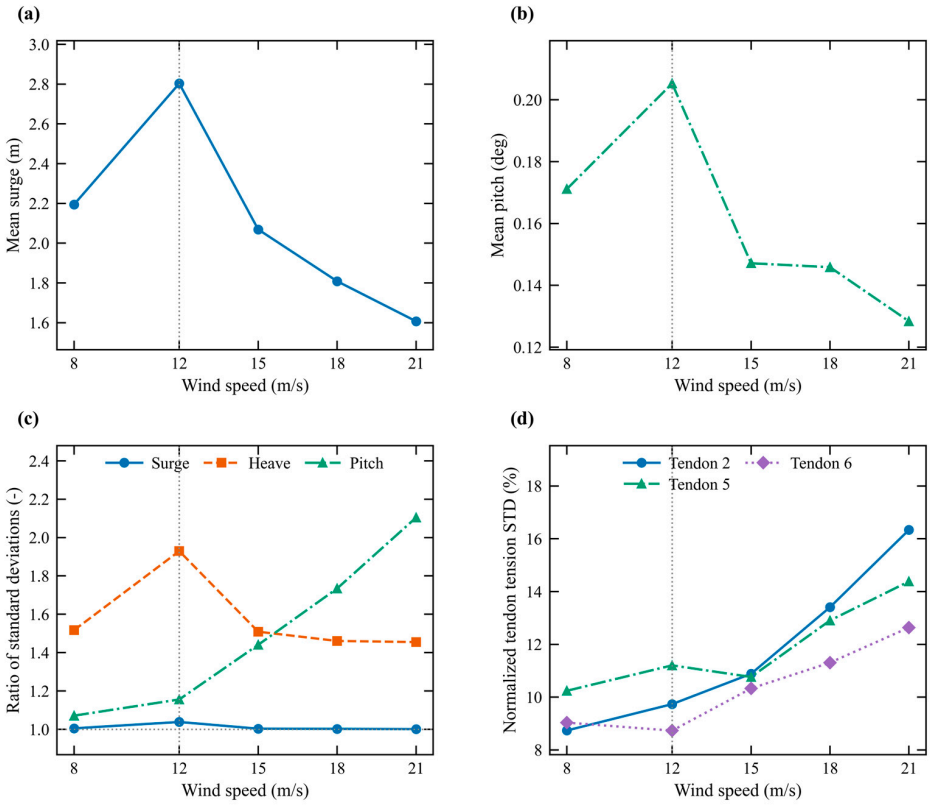


Figure 8. Variations in platform and tendon responses with wind speed at $H_s = 5$ m and $T_p = 12$ s: (**a**) mean value of surge; (**b**) mean value of pitch; (**c**) STD ratios of platform motions; (**d**) normalized STDs of tendon tension.

The fluctuation measures in Figure 8 exhibit distinct wind-speed-dependent trends. The STD ratio for surge remains close to unity throughout the tested wind-speed range. The STD ratio for heave reaches approximately 1.93 at $U = 12$ m/s and remains between 1.45 and 1.51 at the tested above-rated wind speeds. The STD ratio for pitch increases from approximately 1.07 at $U = 8$ m/s to 2.10 at $U = 21$ m/s. For the selected tendons, the normalized tension STDs show variable behavior at the lower wind speeds and increase consistently over $U = 15$–21 m/s. At $U = 21$ m/s, the normalized tension STDs of the selected tendons reach approximately 12.6–16.3%.

The mean values and fluctuation measures in Figure 8 exhibit distinct wind-speed-dependent trends. Oguz et al. [5] associated the reduction in platform offsets above the rated wind speed with the decrease in turbine thrust induced by blade-pitch control. A similar trend is observed in the present tests, where the mean values of surge and pitch decrease above the rated wind speed. In contrast, the STD of pitch increases with wind speed, while the normalized STDs of tendon tension increase consistently over $U = 15$–21 m/s.

To further examine the spatial distribution of tendon loads, Table 8 presents the static pretensions, normalized mean tensions, and normalized tension STDs of all nine tendons under the representative wave-only (H_s = 6 m, T_p = 12 s) and combined wind–wave (U = 12 m/s, H_s = 6 m, T_p = 12 s) conditions. Compared with the wave-only condition, the normalized mean-tension ratios increase by 0.138–0.156 for T1–T3 but decrease by 0.043–0.146 for T4–T9. This redistribution of mean tendon loads is consistent with the wind-induced changes in the mean platform position.

Table 8. Static pretensions, normalized mean tensions, and normalized tension STDs of all nine tendons under representative wave-only and combined wind–wave conditions.

Tendon	T_0 (MN)	Mean/T_0 Wave-Only	Mean/T_0 Wind–Wave	STD/T_0 Wave-Only (%)	STD/T_0 Wind–Wave (%)
T1	7.100	0.955	1.111	11.93	11.42
T2	7.105	0.982	1.120	9.13	11.75
T3	7.094	0.978	1.126	9.55	11.34
T4	7.050	1.022	0.979	7.96	6.31
T5	7.011	1.000	0.905	11.88	12.88
T6	6.997	1.021	0.910	9.44	11.49
T7	6.911	0.989	0.843	9.52	13.75
T8	6.907	0.964	0.919	11.35	10.63
T9	6.916	0.993	0.947	7.67	6.46

3.5. Frequency-Domain Analysis

Frequency-domain analyses were performed for the representative combined wind–wave condition (U = 12 m/s, H_s = 6 m, and T_p = 12 s) and its corresponding wave-only condition. Raw signals within the prototype-scale interval of 500–3000 s were linearly detrended over the entire analysis window, without low-pass or high-pass filtering. Power spectral densities (PSDs) were estimated using Welch's method with a Hann window, a segment length of 512 s, and 50% overlap [41]. Magnitude-squared coherence (MSC) was calculated between synchronized signals using a segment length of 256 s and 50% overlap [42].

Figure 9 compares the PSDs of platform motions under the two loading conditions. The surge PSDs show relatively small differences between the two loading conditions, consistent with the limited change in the STD of surge reported in Section 3.4. The heave PSD is higher under combined loading within approximately 0.56–0.64 Hz. The pitch PSD shows enhanced spectral energy near 0.25 Hz, close to the measured pitch natural frequency of approximately 0.249 Hz.

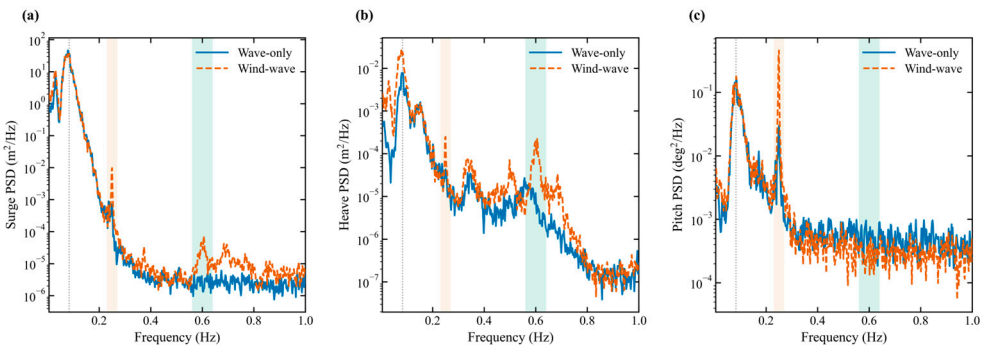


Figure 9. PSDs of platform motions under the representative combined wind–wave condition and the corresponding wave-only condition: (**a**) surge; (**b**) heave; (**c**) pitch. The shaded regions indicate 0.23–0.27 and 0.56–0.64 Hz; the vertical dotted line marks the wave peak frequency.

A coupled numerical study by Li et al. [43] reported that wind excitation increased the low-frequency set-down component and amplified the heave response. This mechanism provides context for the increase in the overall heave response observed here. The localized PSD enhancement at 0.56–0.64 Hz represents a distinct frequency-domain feature and should be interpreted separately from the increase in the overall STD of heave.

Figure 10 shows higher-frequency components in the tendon-tension PSDs, with spectral levels varying among tendon locations. Under combined wind–wave loading, the tendon-tension PSDs show a broad enhancement over approximately 1.0–1.5 Hz relative to the corresponding wave-only condition, with the increase being more evident in T4–T9. Several tendons also exhibit localized spectral features within approximately 2.1–2.2 Hz.

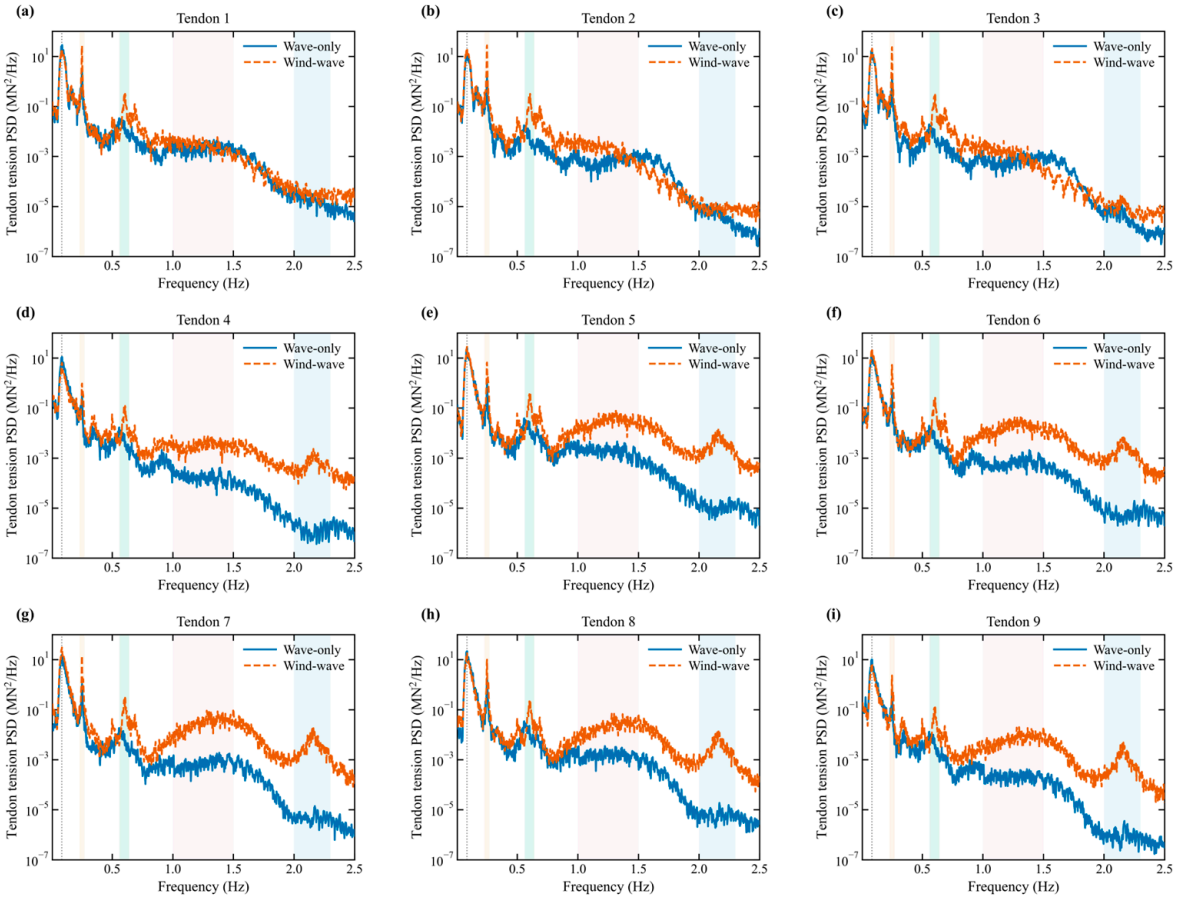


Figure 10. PSDs of tendon tension under the representative combined wind–wave condition and the corresponding wave-only condition: (**a**) T1; (**b**) T2; (**c**) T3; (**d**) T4; (**e**) T5; (**f**) T6; (**g**) T7; (**h**) T8; (**i**) T9. The shaded regions indicate 0.23–0.27, 0.56–0.64, 1.00–1.50, and 2.00–2.30 Hz; the vertical dotted line marks the wave peak frequency.

Figure 11 shows a localized spectral peak in the tower-top x-acceleration PSD within the 2.1–2.2 Hz range. This frequency range contains the measured second natural frequency of the tower, approximately 2.15 Hz, and overlaps the localized features observed in the tendon-tension PSDs in Figure 10, particularly for the lateral tendons. This correspondence motivates further examination of the frequency-specific association between the tower and tendon responses using coherence analysis.

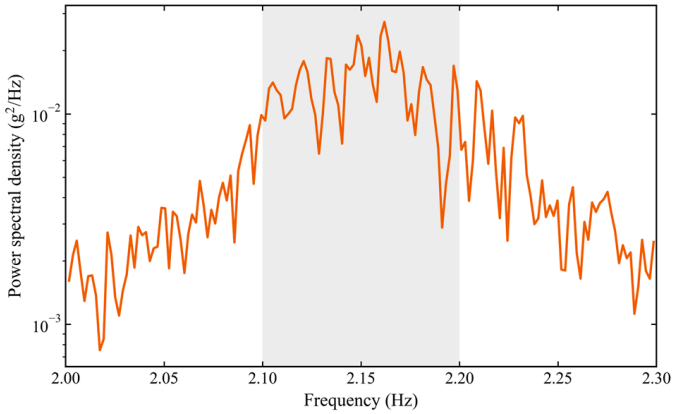


Figure 11. PSD of tower-top x-acceleration under the representative combined wind–wave condition. The shaded region indicates 2.1–2.2 Hz.

Figure 12 shows the MSC between platform pitch and T2 tendon tension. The measured pitch natural frequency of approximately 0.249 Hz is indicated by the vertical dotted line, near which the MSC exhibits a pronounced local maximum. Together with the pitch PSD enhancement near the natural frequency in Figure 9, this coherence maximum indicates a frequency-specific association between the pitch response and T2 tendon tension.

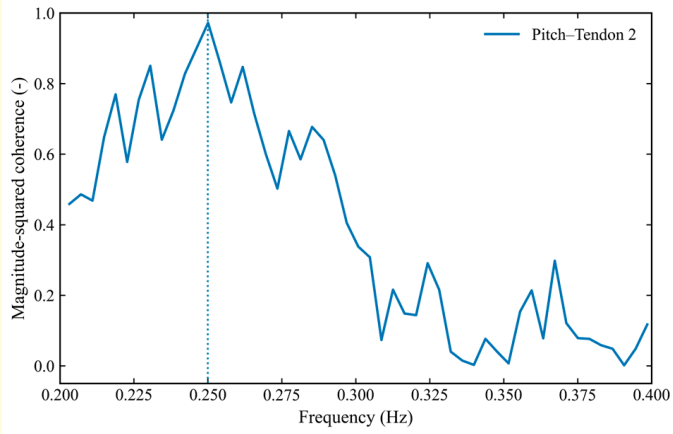


Figure 12. MSC between platform pitch and T2 tendon tension under the representative combined wind–wave condition.

The coincidence of the pitch PSD enhancement and the pitch–T2 coherence maximum near 0.249 Hz suggests that the T2 tendon-tension response may be associated with resonant amplification of pitch near its measured natural frequency.

Figure 13 shows the MSC between tower-top x-acceleration and T5 and T6 tendon tensions. The two MSC spectra exhibit similar shapes, with local maxima of approximately 0.5–0.6 within the 2.1–2.2 Hz range. These maxima occur within the same frequency range as the localized features observed in the tendon-tension and tower-top acceleration PSDs in Figures 10 and 11. The PSD and coherence results therefore support a frequency-specific association between tower-top acceleration and the lateral tendon tensions within this band. Because this frequency range contains the measured second natural frequency of the tower at approximately 2.15 Hz, the observed lateral tendon-tension responses may be associated with resonant amplification of the tower second mode.

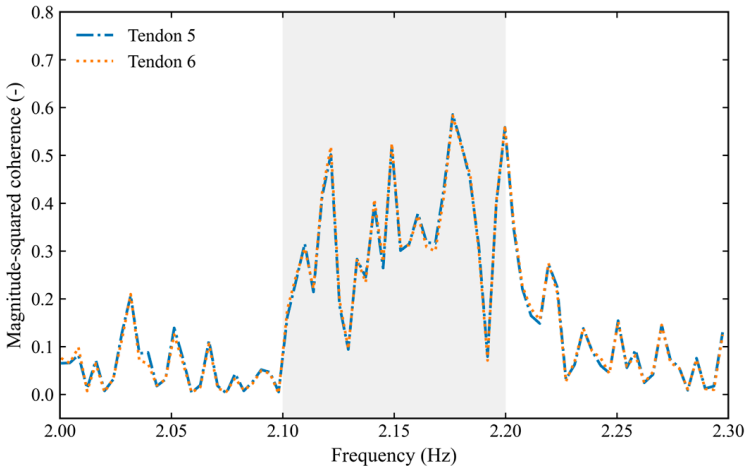


Figure 13. MSC between tower-top x-acceleration and T5/T6 tendon tensions under the representative combined wind–wave condition. The shaded region indicates 2.1–2.2 Hz.

Frequency-domain analysis further identified two distinct coupling features. The upwave tendon T2 may be coupled with the platform pitch response near the measured pitch natural frequency of approximately 0.249 Hz. The lateral tendons T5 and T6 may be coupled with the tower second mode within 2.1–2.2 Hz, suggesting that their higher-frequency tension responses may be associated with resonant amplification of the tower second mode. Although the wave-only and combined wind–wave tests allow comparisons of the overall responses with and without aerodynamic loading, the available experimental data do not permit independent quantification of the contributions of aerodynamic loading, hydrodynamic excitation, and structural configuration to the observed responses.

4. Conclusions

A series of 1:85-scale hybrid model tests, including free-decay, regular-wave, irregular-wave, and combined wind–wave tests, was conducted to investigate the platform motions and tendon tensions of a 16 MW TLP floating wind turbine. The main findings are summarized as follows.

Under wave-only conditions, platform motions and tendon tensions exhibit different sensitivities to wave parameters. Under regular waves, the surge RAO increases toward longer periods, whereas the tendon tension RAOs peak at approximately 9–10 s within the tested range. Under irregular waves, increasing peak period increases surge and heave fluctuations but reduces the normalized tendon-tension fluctuations of the selected tendons, while increasing significant wave height increases both platform and tendon fluctuations.

Combined wind–wave loading affects the mean and fluctuating responses differently. Wind loading introduces mean platform offsets and alters the mean tension distribution among the selected tendons, while the surge fluctuation level remains close to the corresponding wave-only response. Heave and pitch fluctuations are enhanced relative to the corresponding wave-only responses. With increasing wind speed, the mean values of surge and pitch decrease above the rated wind speed, whereas pitch and tendon-tension fluctuations become more pronounced at higher wind speeds. These results indicate that mean platform responses alone are insufficient to characterize dynamic tendon loading.

The frequency-domain results further show that tendon responses are frequency- and location-dependent. The upwave tendon T2 may exhibit coupling with the platform pitch response near the measured pitch natural frequency of 0.249 Hz, whereas the lateral tendons T5 and T6 may exhibit coupling with the tower second mode within 2.1–2.2 Hz.

Overall, the experiments demonstrate that the dynamic response of large-capacity TLP floating wind turbines should be characterized through joint consideration of platform motions and tendon-tension responses. The findings provide experimental insight into the dynamic behavior of the platform–tendon system under wave and combined wind–wave loading, supporting the assessment of large-capacity TLP floating wind turbines under the investigated conditions. The present study focuses on the tested wave-only and normal operating conditions, while future work will investigate the dynamic responses of the platform and tendons under extreme storm conditions.

Author Contributions: Conceptualization, Q.W., X.H. and W.S.; methodology, Q.W., X.H. and W.S.; validation, Q.W., X.H., W.S., C.L. and L.C.; formal analysis, Q.W.; investigation, Q.W., C.L. and L.C.; resources, X.H., W.S., Y.Y., W.Y. and G.C.; data curation, Q.W.; writing—original draft preparation, Q.W.; writing—review and editing, Q.W., X.H., W.S., C.L., L.C., Y.Y., W.Y. and G.C.; visualization, Q.W.; supervision, X.H. and W.S.; project administration, X.H., W.S., Y.Y., W.Y. and G.C.; funding acquisition, X.H. and W.S. All authors have read and agreed to the published version of the manuscript.

Funding: This research was funded by the Ministry of Industry and Information Technology, with internal grant number 2024GXB-FOWT-CTR-009.

Institutional Review Board Statement: Not applicable.

Informed Consent Statement: Not applicable.

Data Availability Statement: The data presented in this study are available from the corresponding author upon reasonable request.

Conflicts of Interest: Authors Yingping Yu, Wendeng Yang, and Guangyuan Cheng were employed by Beijing New Energy Branch, CNOOC (China) Limited. The remaining authors declare that the research was conducted in the absence of any commercial or financial relationships that could be construed as a potential conflict of interest.

References

1. Edwards, E.C.; Holcombe, A.; Brown, S.; Ransley, E.; Hann, M.; Greaves, D. Evolution of floating offshore wind platforms: A review of at-sea devices. *Renew. Sustain. Energy Rev.* **2023**, *183*, 113416. [CrossRef]
2. Papi, F.; Bianchini, A. Technical challenges in floating offshore wind turbine upscaling: A critical analysis based on the NREL 5 MW and IEA 15 MW reference turbines. *Renew. Sustain. Energy Rev.* **2022**, *162*, 112489. [CrossRef]
3. Bachynski, E.E.; Moan, T. Design considerations for tension leg platform wind turbines. *Mar. Struct.* **2012**, *29*, 89–114. [CrossRef]
4. Wang, Y.; Yao, T.; Zhao, Y.; Jiang, Z. Review of tension leg platform floating wind turbines: Concepts, design methods, and future development trends. *Ocean Eng.* **2025**, *324*, 120587. [CrossRef]
5. Oguz, E.; Clelland, D.; Day, A.H.; Incecik, A.; Amate López, J.; Sánchez, G.; González Almeria, G. Experimental and numerical analysis of a TLP floating offshore wind turbine. *Ocean Eng.* **2018**, *147*, 591–605. [CrossRef]
6. Murfet, T.; Abdussamie, N. Loads and response of a tension leg platform wind turbine with non-rotating blades: An experimental study. *J. Mar. Sci. Eng.* **2019**, *7*, 56. [CrossRef]
7. Haider, R.; Shi, W.; Lin, Z.; Xiao, Q.; Zhang, W.; Li, X. Dynamic response of floating offshore wind turbine to focused wave excitation. *Phys. Fluids* **2025**, *37*, 082120. [CrossRef]
8. Subbulakshmi, A.; Verma, M.; Keerthana, M.; Sasmal, S.; Harikrishna, P.; Kapuria, S. Recent advances in experimental and numerical methods for dynamic analysis of floating offshore wind turbines—An integrated review. *Renew. Sustain. Energy Rev.* **2022**, *164*, 112525. [CrossRef]
9. Coulling, A.J.; Goupee, A.J.; Robertson, A.N.; Jonkman, J.M.; Dagher, H.J. Validation of a FAST semi-submersible floating wind turbine numerical model with DeepCwind test data. *J. Renew. Sustain. Energy* **2013**, *5*, 023116. [CrossRef]
10. Koo, B.J.; Goupee, A.J.; Kimball, R.W.; Lambrakos, K.F. Model tests for a floating wind turbine on three different floaters. *J. Offshore Mech. Arct. Eng.* **2014**, *136*, 020907. [CrossRef]
11. Goupee, A.J.; Koo, B.J.; Kimball, R.W.; Lambrakos, K.F.; Dagher, H.J. Experimental comparison of three floating wind turbine concepts. *J. Offshore Mech. Arct. Eng.* **2014**, *136*, 020906. [CrossRef]

12. Vittori, F.; Azcona, J.; Eguinoa, I.; Pires, O.; Rodríguez, A.; Morató, Á.; Garrido, C.; Desmond, C. Model tests of a 10 MW semi-submersible floating wind turbine under waves and wind using hybrid method to integrate the rotor thrust and moments. *Wind Energy Sci.* **2022**, *7*, 2149–2161. [CrossRef]
13. Fowler, M.; Lenfest, E.; Viselli, A.; Goupee, A.; Kimball, R.; Bergua, R.; Wang, L.; Zalkind, D.; Wright, A.; Robertson, A. Wind/wave testing of a 1:70-scale performance-matched model of the IEA Wind 15 MW reference wind turbine with real-time ROSCO control and floating feedback. *Machines* **2023**, *11*, 865. [CrossRef]
14. Zhao, Y.; She, X.; He, Y.; Yang, J.; Peng, T.; Kou, Y. Experimental study on new multi-column tension-leg-type floating wind turbine. *China Ocean Eng.* **2018**, *32*, 123–131. [CrossRef]
15. Madsen, F.J.; Nielsen, T.R.L.; Kim, T.; Bredmose, H.; Pegalajar-Jurado, A.; Mikkelsen, R.F.; Lomholt, A.K.; Borg, M.; Mirzaei, M.; Shin, P. Experimental analysis of the scaled DTU10MW TLP floating wind turbine with different control strategies. *Renew. Energy* **2020**, *155*, 330–346. [CrossRef]
16. Hmedi, M.; Uzunoglu, E.; Medina-Manuel, A.; Mas-Soler, J.; Vittori, F.; Pires, O.; Azcona, J.; Souto-Iglesias, A.; Guedes Soares, C. Experimental analysis of CENTEC-TLP self-stable platform with a 10 MW turbine. *J. Mar. Sci. Eng.* **2022**, *10*, 1910. [CrossRef]
17. Walia, D.; Schünemann, P.; Hartmann, H.; Adam, F.; Großmann, J. Numerical and physical modeling of a tension-leg platform for offshore wind turbines. *Energies* **2021**, *14*, 3554. [CrossRef]
18. Vardaroglu, M.; Gao, Z.; Avossa, A.M.; Ricciardelli, F. Validation of a TLP wind turbine numerical model against model-scale tests under regular and irregular waves. *Ocean Eng.* **2022**, *256*, 111491. [CrossRef]
19. Han, Z.; Zhao, Y.; Su, J.; He, Y.; Xu, Y.; Wu, F.; Jiang, Z. On the hydrodynamic responses of a multi-column TLP floating offshore wind turbine model. *Ocean Eng.* **2022**, *253*, 111262. [CrossRef]
20. Ren, Y.; Shi, W.; Venugopal, V.; Zhang, L.; Li, X. Experimental study of tendon failure analysis for a TLP floating offshore wind turbine. *Appl. Energy* **2024**, *358*, 122633. [CrossRef]
21. Sergiienko, N.Y.; da Silva, L.S.P.; Bachynski-Polić, E.E.; Cazzolato, B.S.; Arjomandi, M.; Ding, B. Review of scaling laws applied to floating offshore wind turbines. *Renew. Sustain. Energy Rev.* **2022**, *162*, 112477. [CrossRef]
22. Chen, C.; Ma, Y.; Fan, T. Review of model experimental methods focusing on aerodynamic simulation of floating offshore wind turbines. *Renew. Sustain. Energy Rev.* **2022**, *157*, 112036. [CrossRef]
23. Azcona, J.; Bouchotrouch, F.; Vittori, F. Low-frequency dynamics of a floating wind turbine in wave tank–scaled experiments with SiL hybrid method. *Wind Energy* **2019**, *22*, 1402–1413. [CrossRef]
24. Urbán, A.M.; Guanche, R. Wind turbine aerodynamics scale-modeling for floating offshore wind platform testing. *J. Wind Eng. Ind. Aerodyn.* **2019**, *186*, 49–57. [CrossRef]
25. Hall, M.; Goupee, A.J. Validation of a hybrid modeling approach to floating wind turbine basin testing. *Wind Energy* **2018**, *21*, 391–408. [CrossRef]
26. Shi, W.; Fu, J.; Ren, Z.; Jiang, Z.; Wang, T.; Cui, L.; Li, X. Real-time hybrid model tests of floating offshore wind turbines: Status, challenges, and future trends. *Appl. Ocean Res.* **2023**, *141*, 103796. [CrossRef]
27. Ha, Y.J.; Ahn, H.; Park, S.; Park, J.Y.; Kim, K.H. Development of hybrid model test technique for performance evaluation of a 10 MW class floating offshore wind turbine considering asymmetrical thrust. *Ocean Eng.* **2023**, *272*, 113783. [CrossRef]
28. Bonnefoy, F.; Leroy, V.; Mojallizadeh, M.R.; Delacroix, S.; Arnal, V.; Gilloteaux, J.C. Multidimensional hybrid software-in-the-loop modeling approach for experimental analysis of a floating offshore wind turbine in wave tank experiments. *Ocean Eng.* **2024**, *309*, 118390. [CrossRef]
29. Meng, H.; Cao, F.; Shi, H.; Li, M.; Li, C.; Chen, Z.; Han, Y.; Chen, P.; Liu, B. Real-time hybrid model experimental and numerical study of a novel 15 MW semi-submersible wind turbine. *Energy Convers. Manag.* **2025**, *346*, 120463. [CrossRef]
30. Fu, J.; Shi, W.; Han, X.; Karimirad, M.; Wang, T.; Li, X. Development and performance study of a multi-degree-of-freedom loading device for real-time hybrid model testing of floating offshore wind turbines. *Mar. Struct.* **2025**, *99*, 103717. [CrossRef]
31. Yang, X.; Zhang, Y.; Yan, S.; Yu, W.; Lu, S.; Wang, H.; Shi, W. Study on motion performance and mooring tension response of 16 MW tension leg platform floating wind turbine under extreme environmental conditions. *J. Mar. Sci. Eng.* **2025**, *13*, 2063. [CrossRef]
32. Li, D.; Deng, X.; Fu, S.; Qu, D.; Gong, W.; Wang, J. Experiment and numerical simulation of dynamic response for a 15-MW tension leg platform FOWT in storm conditions. *J. Ocean Univ. China* **2026**, *25*, 1631–1644. [CrossRef]
33. Qu, D.; Gong, W.; Sun, T.; Chen, Q.; Wang, D.; Wang, J. Tendon inclination effect on the dynamic response and power performance of tension leg platform floating offshore wind turbine. *Ocean Eng.* **2026**, *346*, 123792. [CrossRef]
34. Chen, Q.; Chen, J.; Yang, C.; Wang, S.; Li, G.; Ma, L.; Liu, B.; Liu, Y.; Bai, Z.; Wang, J. Integrated design and experimental–numerical validation of a 22 MW TLP FOWT. *J. Mar. Sci. Eng.* **2026**, *14*, 588. [CrossRef]
35. Yun, S.; Shokati, M.; Kim, J.S.; Ha, Y.J.; Kim, K.H.; Lee, S. Control-induced modification in a tension-leg platform floating wind turbine. *Ocean Eng.* **2026**, *358*, 125592. [CrossRef]
36. Guo, J.; Liu, M.; Pan, X.; Ye, Q.; Su, L.; Chen, W. Experimental study of motion and load responses of a TLP FOWT under combined wind, wave, and current conditions. *Ocean Eng.* **2026**, *347*, 124043. [CrossRef]

37. Bae, Y.H.; Kim, M.H. Rotor-floater-tether coupled dynamics including second-order sum-frequency wave loads for a mono-column-TLP-type FOWT (floating offshore wind turbine). *Ocean Eng.* **2013**, *61*, 109–122. [CrossRef]
38. Sun, S.; Shen, X.; Wang, J.; Li, D. Mechanism of high-frequency response and mooring fatigue in a 15 MW TLP floating offshore wind turbine under second-order sum-frequency wave excitation. *Ocean Eng.* **2026**, *365*, 127199. [CrossRef]
39. Shi, W.; Cao, L.; Ding, H.; Li, C.; Wang, Q.; Han, X.; Leng, Z.; Li, X. AI-enabled real-time hybrid model testing of floating wind turbines: An asynchronous aerodynamic load prediction framework validated on a 16 MW TLP turbine. *Energy* **2026**, *364*, 142379. [CrossRef]
40. Hasselmann, K.; Barnett, T.P.; Bouws, E.; Carlson, H.; Cartwright, D.E.; Enke, K.; Ewing, J.A.; Gienapp, H.; Hasselmann, D.E.; Kruseman, P. *Measurements of Wind-Wave Growth and Swell Decay During the Joint North Sea Wave Project (JONSWAP)*; Deutsches Hydrographisches Institut: Hamburg, Germany, 1973; pp. 1–95.
41. Welch, P.D. The use of fast Fourier transform for the estimation of power spectra: A method based on time averaging over short, modified periodograms. *IEEE Trans. Audio Electroacoust.* **1967**, *15*, 70–73. [CrossRef]
42. Carter, G.C. Coherence and time delay estimation. *Proc. IEEE* **1987**, *75*, 236–255. [CrossRef]
43. Li, Y.; Tang, Y.; Zhu, Q.; Qu, X.; Wang, B.; Zhang, R. Effects of second-order wave forces and aerodynamic forces on dynamic responses of a TLP-type floating offshore wind turbine considering the set-down motion. *J. Renew. Sustain. Energy* **2017**, *9*, 063302. [CrossRef]

Disclaimer/Publisher's Note: The statements, opinions and data contained in all publications are solely those of the individual author(s) and contributor(s) and not of MDPI and/or the editor(s). MDPI and/or the editor(s) disclaim responsibility for any injury to people or property resulting from any ideas, methods, instructions or products referred to in the content.